CP-IRGS: A Region-Based Segmentation of Multilook Complex Compact Polarimetric SAR Data

Mohsen Ghanbari, *Student Member, IEEE*, David A. Clausi, *Senior Member, IEEE*, and Linlin Xu, *Member, IEEE*

***Abstract*—The Canadian RADARSAT constellation mission (RCM) is represented by three synthetic aperture radar (SAR) satellites, each of which includes a compact polarimetry (CP) mode. CP is advantageous because it provides increased backscatter information relative to single and conventional dual-polarized modes and has larger swath widths relative to a quad polarization mode. CP captures single-look complex data which can be used to derive the multilook complex (MLC) coherence matrix, or, equivalently, the Stokes vector data of the backscattered field. The challenge is to develop computer vision algorithms that can be used to effectively segment the scene using this new data source. An unsupervised region-based segmentation approach has been designed and implemented that utilizes the complex Wishart distribution characteristic of the MLC CP data. The segmentation method is based on the iterative region growing with semantics algorithm originally designed for single and dual pol intensity SAR data. The algorithm has been tested using both simulated CP SAR images and a pair of available quad polarization SAR images. The results demonstrate that the CP-IRGS algorithm provides more accurate segmentation images than those using only the RH and RV channel intensity images.**

***Index Terms*—Complex Wishart distribution, Markov random fields (MRFs), multilook complex compact polarimetry, region-based, sea-ice, synthetic aperture radar (SAR), unsupervised segmentation.**

NOMENCLATURE

$\mathbf{E}_{CP}$	Backscattered field in a CP SAR.
E_H, E_V	CP complex measurements.
$\mathbf{J}$	CP MLC coherence matrix.
L	Number of looks.
$\mathbf{B}$	Mathematical expectation of $\mathbf{E}_{CP}\mathbf{E}_{CP}^{*T}$.
$\mathbf{G}$	Scaled MLC coherence matrix.
$T, \mathbf{Q}$	Texture and speckle parameters of the product model.
$\mathbf{x}, \mathbf{y}$	Image data and a label configuration.
$\mathcal{M}$	Label set.
$\mathcal{G}$	Region adjacency graph.
$\mathcal{V}, \mathcal{E}$	Vertices (regions) and edges (boundaries).
ψ_u, ψ_p	Unary and pairwise clique potentials.
$\mathcal{N}_s$	Set of neighbors of site s.
$g(\nabla_s)$	Edge penalty function in site s.
∂v_i	Boundary sites between regions labeled i and other regions.
β	Weight parameter in pairwise potential.
τ_{maxHLT}	Similarity measure between two MLC CP coherence matrices.
C_1, C_2	Weight parameter equation constants.
h	Measure of separability between classes.
$\mathbf{M}_i$	Mean MLC CP coherence matrix of class i.
∂E	Energy difference.
n_i	Number of pixel sites in region i.

Manuscript received January 26, 2021; revised May 25, 2021 and June 8, 2021; accepted June 13, 2021. Date of publication June 23, 2021; date of current version July 14, 2021. This work was supported in part by the Network of Centers of Excellence (ArcticNet), in part by Natural Sciences and Engineering Research Council (NSERC), and in part by the Canadian Ice Service (CIS) of Environment Canada. *(Corresponding author: Mohsen Ghanbari.)*

The authors are with the Vision and Image Processing (VIP) Research Group, Department of Systems Design Engineering, University of Waterloo, Waterloo, ON N2L 3G1, Canada (e-mail: m5ghanba@uwaterloo.ca; dclausi@uwaterloo.ca; linlinxu618@gmail.com).

Digital Object Identifier 10.1109/JSTARS.2021.3089874

I. INTRODUCTION

SYNTHETIC aperture radar (SAR) offers a remote sensing sensor that is used on orbiting satellites to create digital images of the earth's surface. Compact polarimetry (CP) is a SAR mode that offers a compromise between traditional dual polarization (DP) and quad polarization (QP) systems. DP systems offer limited information (two intensity images) but wide (100 s of kilometers) ground swath, whereas QP offers full complex information but narrow swath widths that are not appropriate for large-scale mapping and not useful for operational sea ice mapping [1], [2]. CP is advantageous because it is more informative than DP and provides information close to QP but at wide swaths. Based on this, there has been a trend toward utilization of CP SAR data for a variety of remote sensing applications such as terrain classification [3], oil spill detection [4], and change detection [5].

CP SAR data is acquired using a coherent dual-polarized SAR, where the relative phase between the two received orthogonal linear polarizations in response to a single polarization (commonly circular) is retained. A CP SAR provides many advantages of QP SAR, while requiring simpler system requirements than those of a QP SAR [6]. Many studies have reinforced the concept that classification results from CP are "almost the same" as those from QP data [1], [7]–[9].

A CP SAR maximizes the measurement potential of a radar illumination by providing the capability to derive the four elements of Stokes vector, or equivalently, the 2×2 coherence matrix of the backscattered field [10]. This is the main advantage of a CP SAR over the traditional dual-polarized SARs. Self-calibration capability, less error sensitivity, and comparable signal levels in the two received polarization channels are other advantages of CP SARs [6]. The RADARSAT constellation mission (RCM), which is the successor of the RADARSAT-1

and -2 satellites, includes three satellites that were all launched June 2019. Each satellite, in addition to the QP and DP modes, also has a CP mode that is implemented in wide swaths. This will be utilized extensively by a primary user of this data, the Canadian Ice Service (CIS). CIS experts process 1000 s of SAR scenes annually and manually generate maps of ice regimes on a daily basis. As such, automated methods based on computer vision algorithms for mapping ice regimes using CP SAR data are advocated.

CP data to support classification and segmentation methodologies can be categorized into two main approaches. In the first approach, the four elements of the Stokes vector and all the derived "child parameters" are used as features [7], [8]. In the second approach, based on two target symmetry assumptions, the QP 3×3 covariance matrix is reconstructed using the CP 2×2 coherence matrix. The reconstructed "pseudocovariance" matrix is then used to support the classification algorithm [11].

In this article, a different approach is proposed. Directly using the 2×2 coherence matrix, which is more favorable than using pseudocovariance matrix [12], an unsupervised region-based segmentation method on the basis of the statistical properties of the CP coherence matrix is developed. The region-based segmentation is formulated using Markov random fields (MRFs). A region-based segmentation algorithm uses the statistical properties of regions, and, as a result, is less sensitive to the multiplicative speckle noise and intraclass nonstationarities that are prevalent in wide-swath SAR images. Also, a region-based segmentation method is favorable in computation speed as the number of regions is significantly smaller than the number of pixels. We know of no other published paper that performs unsupervised region-based segmentation of complex CP SAR images.

The region-based segmentation approach proposed in this article is based on a published unsupervised segmentation method called iterative region growing with semantics (IRGS) [13] which has been shown to be successful when applied to generic imagery, hyperspectral imagery, amplitude SAR imagery, as well as complex QP SAR data (PolarIRGS) [14]–[17]. IRGS is based on MRFs and incorporates an edge strength measure in the MRF's spatial context model as well as a novel iterative region-merging process [14]. In an MRF-based segmentation model, using Bayesian inference, the optimal label field is obtained through maximizing the multiplication of conditional probability density function ("feature model" or "likelihood") and the probability of a random field ("spatial context model" or "prior") [17].

In this article, an extension to the IRGS algorithm for CP SAR data is formulated and implemented. The backscattered field in a CP SAR is known to follow a complex Gaussian distribution and, as such, this leads to the multilook CP coherence matrix to be Wishart distributed and this acts as the unary and pairwise potentials of the MRF in the region-based CP-IRGS segmentation method. The statistical significance of differences [18] in CP coherence matrices is used in a novel definition of edge strength and the weight parameter in the pairwise potential of the MRF model. Moreover, based on the assumption that the "product model" [19] is held for the CP backscatter field, a CP coherence matrix data set is simulated and used in the performance evaluation of the proposed segmentation method.

In summary, in this article, we provide a detailed description of the statistical characteristics of the CP data and develop a region-based unsupervised segmentation method for CP data. Our main contributions are as follows.

- Despite the great amount of work in the literature on segmentation/classification using DP and QP SAR data, the studies on segmentation/classification using CP data are limited. Here, for what we expect is the first time in the literature, we propose a region-based approach to unsupervised segmentation of CP data by developing a CP extension of IRGS segmentation methodology.
- In the pairwise potential of IRGS, a new edge strength calculation and weight parameter estimation methods are developed particularly based on the complex CP data type.
- Based on the statistical properties of the complex CP backscatter field data and the product model, a method is proposed to simulate complex CP scenes. The simulated scenes allow for accurately evaluating the proposed unsupervised segmentation method since the boundaries are known.

Section II provides the statistical formulation of the complex CP data. Section III outlines the IRGS algorithm structure. Section IV details the proposed CP-IRGS including the formulation of the MRF data likelihood and the prior term. Section V details the experimental setup, and Section VI describes the simulated and real complex SAR images which are used to evaluate the performance of the CP-IRGS segmentation in Section VII. Conclusions and future work are provided in Section VIII.

II. Multilook Complex CP SAR Statistics

The purpose of this section is to provide the statistical formulation of the multilook complex (MLC) CP coherence matrix data. In a CP SAR, a complex measurement vector $\mathbf{E}$ of the backscattered field is measured. The radar scattering matrix $\mathbf{S}$ relates the incident field to the backscatter one [20]

$$\mathbf{E}_{CP} = \begin{bmatrix} E_H \\ E_V \end{bmatrix} = \mathbf{S}\hat{\mathbf{u}}_t \tag{1}$$

where $\hat{\mathbf{u}}_t$ is the unit Jones vector related to the incident field. Note that the complex measurements in a QP SAR data set are the elements of the scattering matrix $\mathbf{S}$ in (1); therefore, the physical interpretation of complex CP data and complex QP data types are different although they are both represented as complex values. The 2×2 Hermitian positive semidefinite MLC coherence matrix ($\mathbf{J}$) is derived via multiplying $\mathbf{E}_{CP}$ by its complex conjugate transpose [21]

$$\mathbf{J} = \frac{1}{L}\sum_{i=1}^{L} \mathbf{E}_{CP}\mathbf{E}_{CP}^{\dagger} = \begin{bmatrix} \langle |E_H|^2 \rangle & \langle E_H E_V^* \rangle \\ \langle E_V E_H^* \rangle & \langle |E_V|^2 \rangle \end{bmatrix} \tag{2}$$

where $\langle \cdots \rangle$ shows temporal or spatial averaging, $\dagger$ indicates Hermitian conjugate, and L is the number of looks used for averaging.

Since a radar illuminates an area of many random scatterers, the 2D measurement vector $\mathbf{E}_{CP}$ in (1) provided by a CP SAR can be assumed to have a bivariate complex Gaussian

distribution

$$p(\mathbf{E}_{CP}) = \frac{1}{\pi^2 |\mathbf{B}|}\exp\left(-\mathbf{E}_{CP}^{*T}\mathbf{B}\mathbf{E}_{CP}\right) \tag{3}$$

where $\mathbf{B} = \mathscr{E}\{\mathbf{E}_{CP}\mathbf{E}_{CP}^{*T}\}$, in which $\mathscr{E}$ represents the mathematical expectation. $\mathbf{B}$ is called the Hermitian complex covariance matrix. The value $\mathbf{J}$ in (2) is the maximum likelihood estimator and a sufficient estimator for $\mathbf{B}$ [22]. Then, Goodman . [22] showed the matrix $\mathbf{G} = L\mathbf{J} = \sum_{i=1}^{L}\mathbf{E}_{CP_i}\mathbf{E}_{CP_i}^{*T}$ has a complex Wishart distribution. Given that the size of the tuple of complex Gaussian variables in (1.6) in the work by Goodman [22] is equal to 2 (the dimension of vector $\mathbf{E}_{CP}$) here, the probability density function of $\mathbf{G}$ is given by

$$p(\mathbf{G}) = \frac{|\mathbf{G}|^{L-2}}{\pi\Gamma(L)\Gamma(L-1)|\mathbf{J}|^{L}}\exp\left[-\mathrm{tr}\left(\mathbf{J}^{-1}\mathbf{G}\right)\right] \tag{4}$$

where $|\cdot|$ is the determinant operator, $\mathrm{tr}(\cdot)$ represents the trace of a matrix, and Γ is Gamma function. $p(\mathbf{G})$ is defined over the domain $D_{\mathbf{G}}$ where $\mathbf{G}$ is Hermitian semi-definite [22].

A. Simulation Method of MLC CP

Simulating MLC CP scenes allow for accurately evaluating the proposed unsupervised segmentation method since the boundaries are known. A multilook CP coherence matrix data set can be simulated based on the assumption that the "product model" is held for the complex vector of the backscattered field, (1):[1]

$$\mathbf{E}_{CP} = \sqrt{T}\mathbf{Q} \tag{5}$$

where $\mathbf{E}_{CP}$ consists of the CP complex measurements E_H and E_V. In (5), it is indicated that the CP measurements are statistically modeled by the product of two terms: T which is a positive scalar that models the texture (spatial variation in the mean backscatter) and a random variable $\mathbf{Q}$ known as speckle parameter that is assumed to be complex Gaussian distributed.[2] Then, according to (2) and (5), the multilook complex coherence matrix is given by [23]

$$\mathbf{J} = \frac{1}{L}\sum_{i=1}^{L}\mathbf{E}_{CP}(l)\mathbf{E}_{CP}^{\dagger}(l) = \frac{1}{L}\sum_{l=1}^{L}T(l)\mathbf{Q}(l)\mathbf{Q}^{\dagger}(l). \tag{6}$$

Assuming the texture does not vary in a resolution cell, $T(l) = T$. Based on the assumption that $\mathbf{Q}$ has a complex Gaussian distribution, as discussed earlier, the matrix $\sum_{l=1}^{L}\mathbf{Q}(l)\mathbf{Q}^{\dagger}(l)$ becomes complex Wishart distributed. Therefore, depending on the probability distribution of T in (5) that is chosen based on the homogeneity of the scene, the MLC CP coherence matrix $\mathbf{J}$ obeys different parametric distributions [24]. The simplest case is for homogeneous areas where texture is assumed to be constant. Other probability distributions such as Gamma and generalized inverse Gaussian were also considered in the literature to model the texture parameter in the heterogeneous and extremely heterogeneous areas, respectively [25].

[1]This assumption is valid when the mean number of scatterers that contribute to a pixel measurement in a CP image is large. For more description, refer to the work by Olivier *et al.* [19].

[2]This is the more general case of what discussed earlier where we mentioned the CP complex measurements $\mathbf{E}_{CP}$ has a complex Gaussian distribution.

III. Background

This section summarizes the fundamental steps of the IRGS segmentation algorithm [13]. Let $\mathcal{S}$ be the image and $s \in \mathcal{S}$ be a site on the image (an image pixel). Also, assume that $\mathbf{x} = \{x_s | s \in \mathcal{S}\}$ represents the image data and $\mathbf{y} = \{y_s | y_s \in \mathcal{M}, s \in \mathcal{S}\}$ is a label configuration on the image with discrete-valued random variables y_s having a value from the label set $\mathcal{M} = \{1, \ldots, m\}$. The purpose of an image segmentation is essentially to find the optimum label configuration. IRGS is formulated based on the Bayesian theory where the objective is to find a label configuration $\mathbf{y}^*$ that satisfies

$$\mathbf{y}^* = \arg\max_{\mathbf{y}\in\mathbf{Y}} p(\mathbf{x}|\mathbf{y})P(\mathbf{y}) \tag{7}$$

where $\mathbf{Y}$ is the set of possible label configurations. The term $p(\mathbf{x}|\mathbf{y})$ is called the feature model or data likelihood and is the conditional probability density function of the image data $\mathbf{x}$ given the label configuration $\mathbf{y}$. $P(\mathbf{y})$ indicates the prior also called the spatial context model. IRGS is a region-based method which uses a region adjacency graph (RAG) [26] and aims to find the optimum label field over a RAG instead of all the image sites separately. A RAG is defined as $\mathcal{G} = (\mathcal{V}, \mathcal{E})$, where $\mathcal{V}$ and $\mathcal{E}$ denote the image regions as vertices and arcs that are the boundaries of adjacent regions. Thus, a region $v \in \mathcal{V}$ in the image consists of a set of image sites $\mathcal{S}_v$.

In IRGS, a Gaussian mixture model [17] is used to model $p(\mathbf{x}|\mathbf{y})$ with an expectation-maximization (EM) algorithm to estimate the parameters of the Gaussian mixture. Also, the spatial context model $P(\mathbf{y})$ is defined using an edge strength measure [13]. By taking a logarithm and multiplying the terms in (7) by -1,[3] the problem is converted to the minimization of two energy terms

$$\mathbf{y}^* = \arg\min_{\mathbf{y}\in\mathbf{Y}}\{-\sum_{\mathcal{S}_v\in\mathcal{V}}\sum_{s\in\mathcal{S}_v}\psi_u(x_s, y_s) - \sum_{\mathcal{S}_v\in\mathcal{V}}\sum_{s\in\mathcal{S}_v}\sum_{n\in\mathcal{N}_s}\psi_p(y_s, y_n)\} \tag{8}$$

where ψ_u and ψ_p are called the unary and pairwise clique potentials. The unary potential is summed up over all sites in the vertex $\mathcal{S}_v$, which is the region that includes the site s, from set $\mathcal{V}$, and the pairwise potential is summed up over all the pair sites s and n, where $\mathcal{N}_s$ is the set of neighbors of the site s. By substituting the corresponding spatial context model in IRGS [13]

$$\mathbf{y}^* = \arg\min_{\mathbf{y}\in\mathbf{Y}}\{-\sum_{i=1}^{m}\sum_{\mathcal{S}_v\in v_i}\sum_{s\in\mathcal{S}_v}\ln\{p(\mathbf{x}_s|y_s = i)\} + \beta\sum_{i=1}^{m-1}\sum_{j=i+1}^{m}\sum_{s\in\partial v_i\cap\partial v_j}g(\nabla_s)\} \tag{9}$$

where $g(\nabla_s)$ is called the edge penalty term [17], v_i is a subset of $\mathcal{V}$ with label i, and ∂v_i indicates all the boundary sites between regions labeled i with other regions. Thus, $\partial v_i \cap \partial v_j$ denotes all the boundary sites between classes i and j. In the first term

[3]The terms are multiplied by -1 to convert the probability maximization problem to an energy minimization problem.

on the right side of (9), $p(\mathbf{x}_s|y_s = i)$ is the probability value of obtaining $\mathbf{x}_s$ given the label of the site s is i. This term is modeled by a Gaussian mixture model in IRGS [13]. In the second term, the edge penalty function $g(\nabla_s)$ is a monotonically decreasing function (when the edge strength for a specific boundary site is high, the penalty is low) that generates a sequence of edge penalties for each iteration of the algorithm [13]. The parameter β controls the smoothness of the segmentation with the greater values of β leading to smoother segmentation results.

IRGS uses a simulated annealing (SA) algorithm to solve the combinatorial optimization problem in (9). Also, in each iteration before the optimization by SA, IRGS performs a region-merging process to reduce the number of regions and to avoid being trapped in a local minima [13], [14]. In summary, after constructing RAG on the "deliberate" oversegmentation image obtained by the watershed algorithm [27], IRGS starts its iterations. In each iteration, SA assigns a label to each region to move the label configuration toward the optimal solution. Adjacent regions that have the same class labels are then merged in a greedy fashion using a merging criterion ∂E [13], and, afterwards, the next iteration is executed.

PolarIRGS, the extension to IRGS for QP SAR data, was developed by Yu *et al.* [17]. Based on Wishart distribution, the unary potential was derived in PolarIRGS. The data input in PolarIRGS is the complex QP data which is different than the complex CP data in terms of physical interpretation. The complex QP data is derived from the elements of scattering matrix [$\mathbf{S}$ in (1)]; however, the complex CP data is extracted from the complex backscattered field [$\mathbf{E}_{CP}$ in (1)]. These two data types are related by (1) as discussed in Section II. The unary based on complex Wishart distribution and the region merging criterion [17] are used here by modifying the data type to complex CP data and new methods are proposed for the calculation of edge penalty and the weight parameters in the pairwise potential.

IV. CP-IRGS

In this section, we describe the formulation of the proposed algorithm based on the complex Wishart distribution. In Sections IV-A and IV-B, we will define the unary and pairwise clique potentials in (8) of CP-IRGS.

A. Complex CP-Based Unary Potential

The data likelihood term $p(\mathbf{x}_s|y_s = i)$in (9) is defined here for MLC coherence matrix data. For each site s in an MLC CP image, the observation data x_s is the MLC coherence matrix, i.e., $x_s = \mathbf{G}_s$, where $\mathbf{G}_s = L\mathbf{J}_s$ was shown in Section II to have a complex Wishart distribution. Therefore, the conditional probability of obtaining $\mathbf{x}_s$ given the site s is labeled y_s, $p(\mathbf{x}_s|y_s)$, is given by[4]

$$p(\mathbf{J}_s|y_s) = \frac{L^{2\tilde{}L}|\mathbf{G}_s|^{L-2}}{\pi\Gamma(L)\Gamma(L-1)\left|\mathbf{J}_{y_s}\right|^{L}}\exp\left[-L\text{tr}\left(\mathbf{J}_{y_s}^{-1}\mathbf{G}_s\right)\right] \tag{10}$$

[4]Note that the probability function in (10) directly models the MLC CP coherence matrix $\mathbf{J}$, and it is slightly different than (4). The probability function in (10) is often called the *scaled* complex Wishart distribution [25].

where $\mathbf{J}_{y_s}$ is the average MLC coherence matrix for all the sites labeled y_s. According to (8) and (9), the unary potential term in CP-IRGS is given by

$$\psi_u(x_s, y_s) = \ln\{p(\mathbf{J}_s|y_s)\}. \tag{11}$$

By taking the natural logarithm of $p(\mathbf{J}_s|y_s)$ in (10), and eliminating all the elements that are not a function of y_s, the unary term is given by [17]

$$\psi_u(x_s, y_s) = \sum_{\mathcal{S}_v\in\mathcal{V}}\sum_{s\in\mathcal{S}_v}\{\ln|\mathbf{J}_{y_s}| + \text{tr}\left(\mathbf{J}_{y_s}^{-1}\mathbf{G}_s\right)\}. \tag{12}$$

B. Complex CP-Based Pairwise Potential

We define the pairwise potential in CP-IRGS as

$$\psi_p(y_s, y_n) = \begin{cases}\beta g(\bigtriangledown_s) & \text{different labels}\\ 0 & \text{otherwise}\end{cases} \tag{13}$$

where "different labels" means that the sites s and n are labeled differently. $\bigtriangledown_s$ is the edge strength measure at the site s, and the edge penalty function $g(\bigtriangledown_s)$ is defined as in the original IRGS algorithm [13, (18)]:

$$g(\bigtriangledown_s) = \exp\left[-\left(\frac{\bigtriangledown_s}{K(i)}\right)^2\right] \tag{14}$$

where $K(i)$ is a positive coefficient that monotonically increases with the iteration number i to control the effect of the edge penalty term ([13, Section 3.1]). At a conceptual level, (13) increases the pairwise potential by $\beta g(\bigtriangledown_s)$ if adjacent regions are of different labels, and in this manner, penalizes segmentations where neighboring regions have weak edges and different labels. The proposed methods of calculating $\bigtriangledown_s$ and the parameter β are described as follows.

1) Calculating Edge Strength: Measuring the edge strength $\bigtriangledown_s$ in each site s can essentially be considered as an edge detection problem. Two edge strength calculation methods are developed. In the first method, following the previous IRGS papers [13], [17], the intensity values in the RH and RV CP channels are used in the vector field gradient (VFG) method [28]. The second method is to develop an edge strength measure that uses the MLC CP coherence matrix data as its input. We propose to use the ratio-based edge detectors [29]–[31] with a complex-CP based *similarity* measure. As shown in Section II, since the MLC CP coherence matrix shares statistical properties with the QP MLC covariance matrix, all the similarity measures for the QP covariance matrices are immediately applicable to the CP coherence matrices.

The ratio-based detectors [29], [31] use a rectangle bi-window configuration shown in Fig. 1. In particular, as shown in Fig. 1, the bi-window configuration consists of two parallel rectangles which are specified by two parameters: length l_f and width w_f, a spacing parameter d_f, and an orientation angle θ_f. Touzi *et al.* [29] proposed using the ratio of mean intensity values in SAR images, and operating a constant false alarm rate afterwards. This algorithm is called likelihood test ratio, and has also been expanded for the QP SAR images [31]. Here, we use the Hotelling–Lawley trace (HLT) [32] as the similarity measure. The HLT statistic can be considered as the matrix-variate version of the intensity ratio test [32]. The HLT measure has shown to

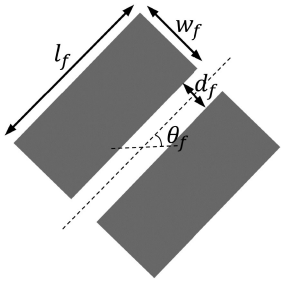

Fig. 1. Bi-window configuration used in the edge strength map calculation.

be an effective test statistic compared to the measures such as Kullback–Leibler divergence in the problem of change detection using the MLC QP covariance matrix data [33]. The HLT statistic measures the similarity between two complex matrix-variates $\mathbf{J}_1$ and $\mathbf{J}_2$

$$\tau_{\text{HLT}} = \text{tr}(\mathbf{J}_1^{-1}\mathbf{J}_2) \tag{15}$$

where $\mathbf{J}_1$ and $\mathbf{J}_2$ are two mean MLC CP coherence matrices in the two rectangles in Fig. 1. Note that τ_{HLT} becomes the intensity ratio when $\mathbf{J}_1$ and $\mathbf{J}_2$ are two scalars indicating intensity values. In the case $\mathbf{J}_1 = \mathbf{J}_2$, the HLT statistic equals the dimension of a complex CP coherence matrix, i.e., $\tau_{\text{HLT}} = 2$. In the case of "dissimilar" $\mathbf{J}_1$ and $\mathbf{J}_2$, τ_{HLT} obtains values distant from d. Based on the type of difference in the two mean coherence matrices, τ_{HLT} can obtain positive values either "smaller" or "much larger" than the dimension of a complex CP coherence matrix [33]. Therefore, the maximum value of $\text{tr}(\mathbf{J}_1^{-1}\mathbf{J}_2)$ and $\text{tr}(\mathbf{J}_2^{-1}\mathbf{J}_1)$ is used here as the test statistic

$$\tau_{\text{maxHLT}} = \max\{\text{tr}(\mathbf{J}_1^{-1}\mathbf{J}_2), \text{tr}(\mathbf{J}_2^{-1}\mathbf{J}_1)\}. \tag{16}$$

Finally, considering there are n_θ different orientation angles, we take the minimum value of τ_{maxHLT} from all the orientations

$$\tau_{\text{total}} = \min_{i=1,\ldots,n_\theta} \{\tau^{\text{i}}_{\text{maxHLT}}(\mathbf{J}_1, \mathbf{J}_2)\} \tag{17}$$

where $\tau^{\text{i}}_{\text{maxHLT}}$ is the τ_{maxHLT} value for the ith orientation. Each orientation angle i corresponds to a pair of mean MLC coherence matrices $\mathbf{J}_1$ and $\mathbf{J}_2$ (from the two rectangles in the bi-window configuration). For each i, the "dissimilarity" between the two mean MLC coherence indicates that there is a change in radar backscatter in that orientation. Taking the minimum value of all the dissimilarity values from different orientations captures the smallest changes in backscatter values in all orientations.

2) Estimating the Weight Parameter β: The weight parameter β in the pairwise potential, (13), should be estimated in each iteration of the algorithm. In the standard IRGS [13], the parameter β is determined by the boundary length expected over the whole image, and, then, it is adjusted to be adaptive to the noise strength of the image. In particular, in each iteration t, a value $\beta_0(t)$ is estimated as a prior via maintaining the expectation of the boundary length the same as the current [13], [34]. To incorporate the noise strength in each iteration of the segmentation into the parameter β, Yu and Clausi [13, (23) and (24)] used the Fisher criterion as a separability measure between any pair of classes in the image for adjusting the prior

Algorithm 1: CP-IRGS Algorithm.

Input: Set C_1 and C_2 in (18), number of classes m, and maximum number of iterations $t_{\max}$.
Output: Segmentation image with c classes.
Initialization:
1: Compute the edge strength τ_{total} in (17) for each site in the image.
2: Apply watershed to obtain an oversegmentation and construct a RAG with each watershed region as a vertex.
3: Assign a random label to each watershed region.
4: Apply a region-based K-means [16] to obtain an initial segmentation from which the average MLC coherence matrix for each class is calculated.
LOOP Process
5: **for** $t = 1$ to $t_{\max}$ **do**
6: Update β and K.
7: Scan all the vertices in a random manner and assign a label to each vertex that minimizes energy terms in $\mathbf{y}^*$, (9).
8: **Repeat:** While all $\partial E \geq 0$
9: Compute ∂E in (20) for all adjacent regions that have the same label.
10: Merge the region pair with the most negative ∂E.
11: **end for**

$\beta_0(t)$. Here, we use τ_{maxHLT} statistic

$$\hat{\beta}(i) = C_1 \frac{h}{C_2 + h}\beta_0(i) \tag{18}$$

where $\hat{\beta}(t)$ represents the adjusted weight parameter, C_1 and C_2 are two constants, and h is given by

$$h = \min_{i,j}\{\tau_{\text{maxHLT}}(\mathbf{M}_i, \mathbf{M}_j)\} \tag{19}$$

where h is a measure of separability between all pairs of classes i and j with respect to the mean value of the MLC CP coherence matrices of the two classes $\mathbf{M}_i$ and $\mathbf{M}_j$.

C. Region Merging Criterion

One of the main features of the IRGS algorithm is incorporating a region-merging technique in each iteration of the optimization. Starting from an oversegmentation, a region-merging process is executed in each iteration. Only for all pairs of the neighboring regions with the same labels, the energy terms in (9) for two cases are calculated: (1) merging the two regions and (2) keeping the regions separate. If the merged case reduces the energy, the regions are merged. The region merging criterion is given by

$$\partial E(i,j) = n_{ij}\ln|\mathbf{M}|_{ij} - n_i \ln|\mathbf{M}_i| - n_j \ln|\mathbf{M}_j| - \beta \sum_{s\in\partial v_i \cap \partial v_j} g(\nabla_s) \tag{20}$$

where $\partial E(i,j)$ is the energy difference between before and after merging, n_i is the number of pixel sites in region i, and ij denotes the region obtained from merging regions i and j. $\mathbf{M}_j$ is the average MLC CP coherence matrix of region i.

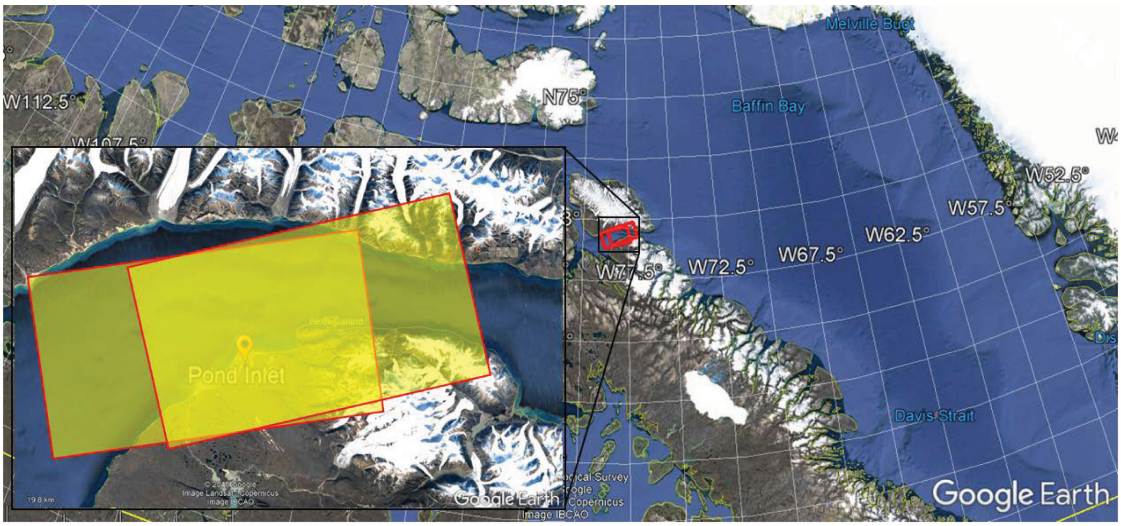

(a)

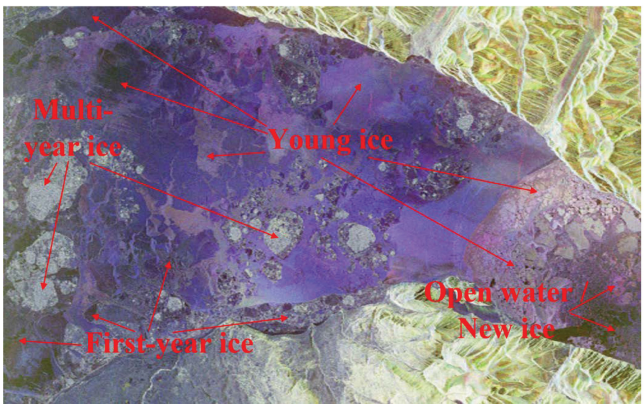

(b)

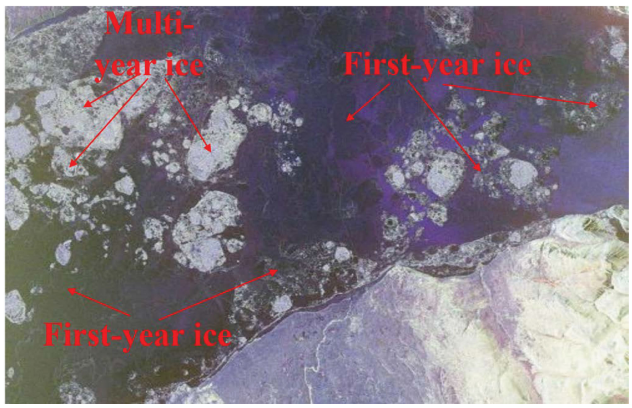

(c)

Fig. 2. (a) The locations of the two RADARSAT-2 fine QP scenes in the Pond Inlet. The Pauli RGB composites (Red: $|HH - VV|$; Green: $2|HV|$; Blue $|HH + VV|$) of scenes (b) Dec16 and (c) Jan17. Example ice types in the scenes are labeled.

D. CP-IRGS Algorithm Overview

An overview of the CP-IRGS algorithm is shown in Algorithm 1. After an oversegmentation using the watershed algorithm [27], a RAG is constructed. To start the algorithm, an initialization is required to input into the algorithm. Through this initialization, each region is assigned a label and, then, the mean MLC CP coherence matrix for each class is computed. The initialization image is obtained via applying a region-based K-means algorithm [16] on the RH and RV channel intensity images.

CP-IRGS is executed in two main nested loops. The outer loop guides the segmentation to the optimal configuration. In each iteration of this loop, the parameter β in (18) and K in (14) are updated. Then, all the vertices in the RAG are assigned a label, (9). In particular, via a SA algorithm, all the vertices in the RAG are scanned in a random manner, and each vertex is assigned a label that minimizes the energy terms in (9). The inner loop executes the region growing process. In each iteration of the inner loop, for all the neighboring pairs of regions that have the same class label, the criterion ∂E in (20) is computed. The region pair with the most negative ∂E is merged. The inner loop ends when there is no adjacent pair with the same label that has $\partial E < 0$.

V. Experimental Setup

An unsupervised segmentation algorithm is expected to produce an image where each pixel is assigned to a particular class with an unknown label. A labeling step is usually followed to assign ground truth labels (the actual class labels of the scene) to the regions in the image [36], [37]. Since the objective of this article is unsupervised segmentation, to evaluate the algorithm without any uncertainties due to an imperfect labeling process, the segmentation regions are assigned labels based on the fully labeled ground truth image of the scenes.

Each class in the unsupervised segmentation image is assigned a label via a majority voting process on the ground truth labels of the pixels inside the class. In other words, in each segmentation class, the number of pixels with each label in the ground truth image is counted and all the regions of the segmentation class is assigned the label associated with the maximum number of pixels. An accurate segmentation provides

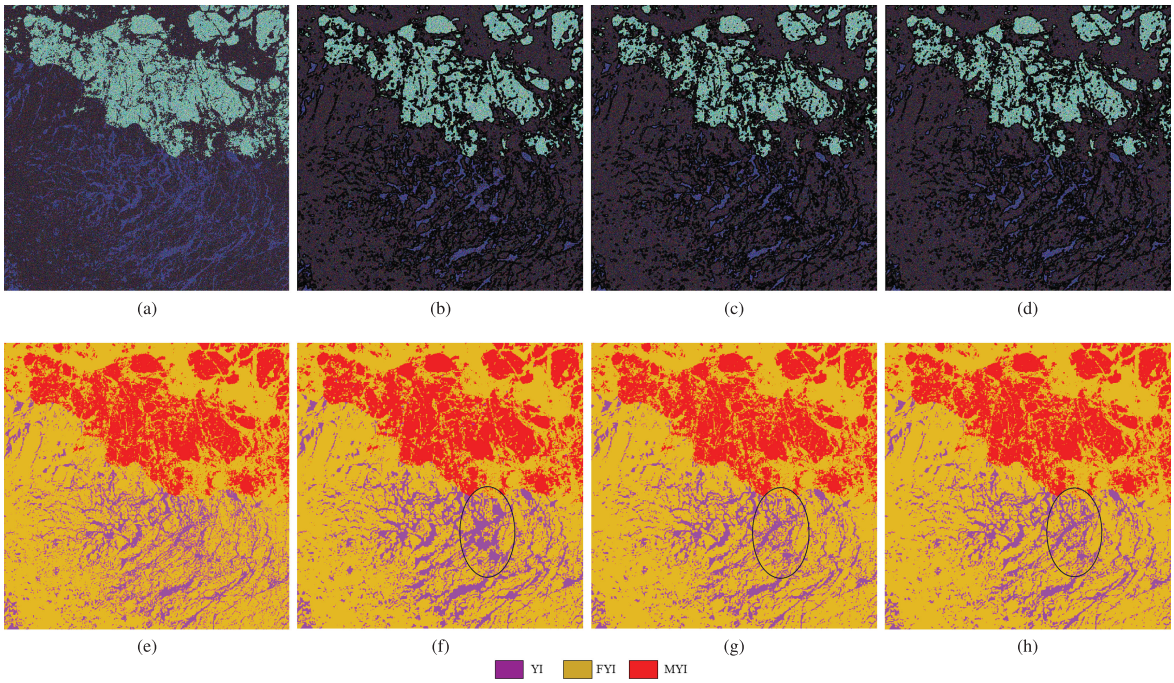

Fig. 3. (a) The $M-\chi$ [35] RGB composite, R $=\sqrt{(mS_0-S_3)/2}$ $G=\sqrt{S_0(1-m)}$ $B=\sqrt{(mS_0+S_3)/2}$, where S_0, S_1, S_2, S_3 are the Stokes parameters and $m=\sqrt{S_1^2+S_2^2+S_3^2}/S_0$ is the degree of polarization. (b)–(d) Unsupervised segmentation boundaries overlaid on top of $M-\chi$ RGB image. (e) Ground truth. (f)–(h) Labeled images of the simulated MLC CP coherence data for (second column to last column) original IRGS segmentation using RH and RV images, CP-IRGS segmentation using the VFG method, and CP-IRGS using the CR-based method. The ovals in the labeled images indicate that a fairly large number of FYI pixels in the middle of the scene are mislabeled as YI using original IRGS.

segmentation classes that are homogeneous, i.e., each class in the segmentation image contains areas only from one ground truth class.

After labeling, the overall accuracy (OA), the accuracy of each class, and the Kappa coefficient (κ) are computed as accuracy measures of the algorithm. Moreover, to measure the effectiveness of the region merging in the unsupervised segmentation algorithm, the total number of regions in the segmentation image is counted. Favorably, the segmentation algorithm should produce images where the regions are as homogeneous as possible (i.e., high accuracy values) and the number of regions is as low as possible.

Three cases are tested and compared.

- Case 1: The standard IRGS method [13] using the RH and RV intensities.
- Case 2: The CP-IRGS method described in Algorithm 1 using VFGs [28] method on the RH and RV intensities for edge strength map calculation.
- Case 3: The CP-IRGS method using edge strength map method described in Section IV-B, which will be referred to as the CP-IRGS using complex ratio (CR)-based method.

The IRGS method in Case 1 uses only the CP channel intensities. In Case 2, the CP-IRGS method uses the MLC CP coherence matrix data in the unary potential, however, in the pairwise potential, the CP channel intensities are used in the VFG. In Case 3, both the unary and pairwise potentials are calculated based on the MLC CP coherence matrix data. The data sets will be described in the next section, and the experiments and analyses are provided afterwards.

TABLE I
ELEMENTS OF THE MEAN MLC CP COHERENCE MATRICES

Class	$\mathbf{J}_{11}$	$\mathbf{J}_{12}$	$\mathbf{J}_{22}$
OW/NI	0.0069	0.0008-0.0056j	0.0118
YI	0.0400	0.0032-0.0272j	0.0407
FYI	0.0167	0.0006-0.0106j	0.0163
MYI	0.0549	0.0040-0.0338j	0.0556

VI. DATA SETS

The unsupervised segmentation methods were evaluated by a simulated MLC CP data set as well as a pair of QP sea-ice scenes that were used to derive the CP data.

A. Simulated MLC CP Data

In this section, a multilook CP coherence matrix data set of sea-ice with 1500×1500 pixels were simulated based on the assumption that the texture is constant and the mean coherence matrix for each class was derived from a real CP SAR scene. The mean coherence matrices for sea-ice classes are presented in Table I. The class boundaries of a real SAR sea-ice scene were used for the simulated MLC CP image, and, then, the regions of each class were populated by the corresponding simulated pixel values of the MLC coherence matrix.

B. MLC CP Images

Two RADARASAT-2 single-look complex (SLC) QP images are used for testing. The images are acquired over Pond Inlet

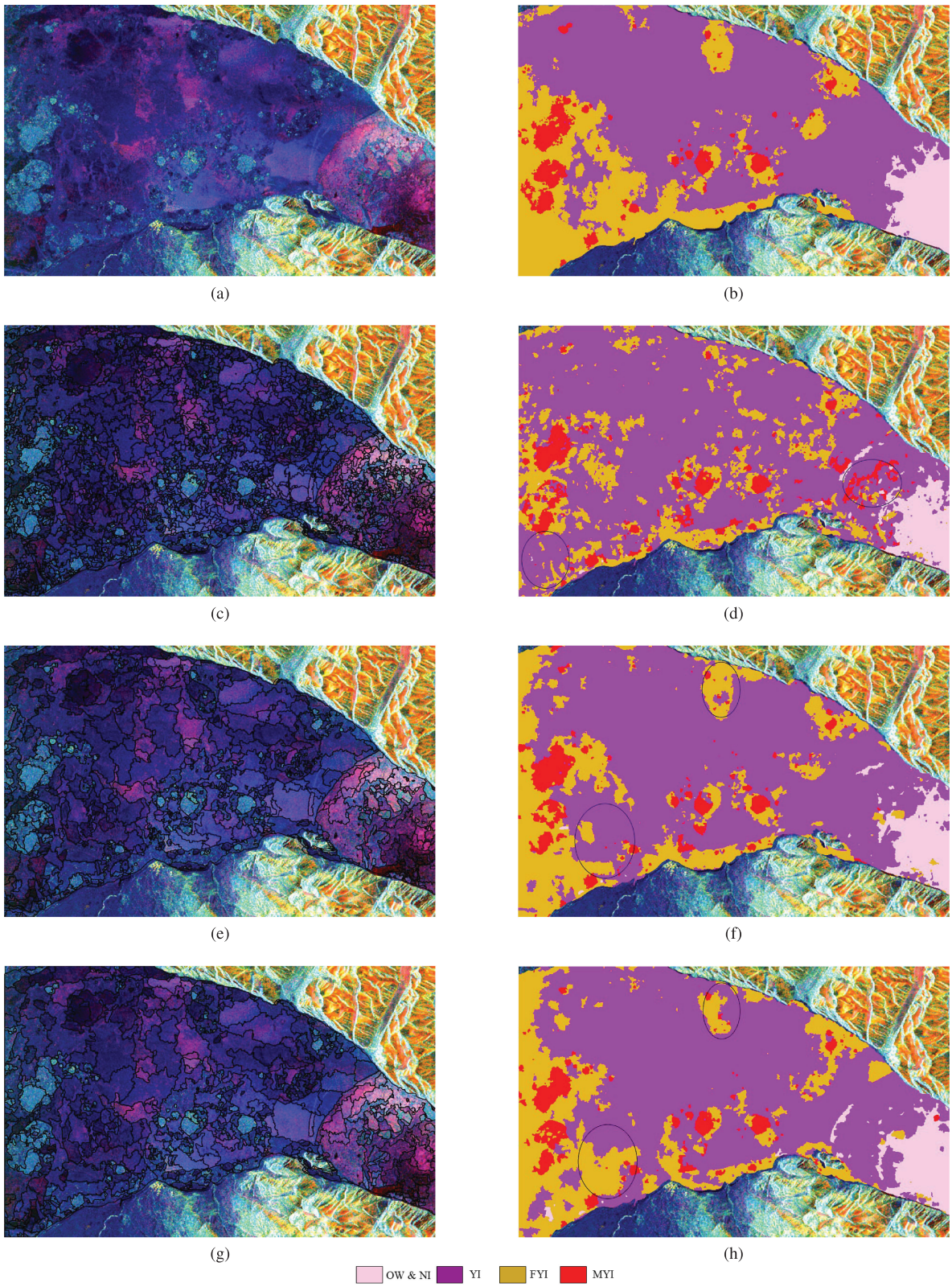

Fig. 4. Scene Dec16. (a) $M-\chi$ decomposition RGB composite; R $= \sqrt{(mS_0 - S_3)/2}$; $G = \sqrt{S_0(1-m)}$; $B = \sqrt{(mS_0 + S_3)/2}$, where S_0, S_1, S_2, S_3 are the Stokes parameters and $m = \sqrt{S_1^2 + S_2^2 + S_3^2}/S_0$ is the degree of polarization. (b) Ground truth, the unsupervised segmentation boundaries overlaid on top of $M-\chi$ RGB image, and the labeled images overlaid on top of land masks for the cases. (c) and (d) Unsupervised IRGS segmentation using RH and RV intensity images. (e) and (f) Unsupervised CP-IRGS segmentation using VFG method. (g) and (h) Unsupervised CP-IRGS segmentation using CR-based method. The ovals in the labeled image (d) indicate mislabeled areas in the scene that are correctly labeled using CP-IRGS. (f) and (h) The ovals in the labeled images (f) and (h) show the differences of CP-IRGS performance using VFG and CR-based methods.

TABLE II
SEGMENTATION METHOD, CLASS ACCURACY VALUES, OVERALL ACCURACY, AND κ COEFFICIENT, AS WELL AS THE NUMBER OF REGIONS IN EACH SEGMENTATION IMAGE FOR THE SIMULATED AND TWO RADARSAT-2 SCENES

Data Set	Measure	Class	IRGS Using RH and RV	CP-IRGS Using VFG	CP-IRGS Using CR
Simulated Scene	User's Accuracy	OW/NI	-	-	-
		YI	80.03	**90.32**	89.23
		FYI	**97.71**	97.06	96.86
		MYI	95.69	**99.31**	98.37
	Overall Accuracy (%)		94.78	**96.72**	96.26
	Kappa Coefficient		0.90	**0.93**	0.92
	Number of Regions		4285	4144	**3794**
Scene Dec16	User's Accuracy	OW/NI	78.34	86.16	**87.49**
		YI	60.76	**71.37**	71.24
		FYI	60.11	76.94	**82.76**
		MYI	88.99	**90.26**	86.93
	Overall Accuracy (%)		74.63	82.58	**83.27**
	Kappa Coefficient		0.49	0.66	**0.68**
	Number of Regions		3779	1063	**953**
Scene Jan17	User's Accuracy	OW/NI	-	-	-
		YI	-	-	-
		FYI	98.06	**99.45**	99.29
		MYI	**92.25**	85.60	90.48
	Overall Accuracy (%)		97.48	97.76	**98.29**
	Kappa Coefficient		0.87	0.89	**0.91**
	Number of Regions		2816	2213	**2069**

TABLE III
SEGMENTATION METHOD, OVERALL ACCURACY, AND κ COEFFICIENT, AS WELL AS THE NUMBER OF REGIONS IN EACH SEGMENTATION IMAGE FOR THE SIMULATED AND TWO REAL MLC CP SCENES. THE COMPARISON OF SEGMENTATION RESULTS USING CP RH AND RV INTENSITIES VERSUS $M-\chi$ PARAMETERS

Data Set	Measure	IRGS RH, RV	IRGS $M-\chi$	CP-IRGS VFG RH, RV	CP-IRGS VFG $M-\chi$
Simulated Scene	OA (%)	94.78	96.07	96.72	96.16
	Kappa	0.90	0.92	0.93	0.85
	No Regions	4284	3751	4144	4206
Scene Dec16	OA (%)	74.63	76.08	82.57	84.57
	Kappa	0.49	0.54	0.66	0.70
	No Regions	3779	5642	1063	1089
Scene Jan17	OA (%)	97.48	96.66	97.76	96.16
	Kappa	0.87	0.81	0.89	0.77
	No Regions	2816	2858	2213	2247

located in Northern Baffin Island. Pond Inlet is of importance in the Arctic in terms of sea-ice mapping support as it has the largest community in Northern Baffin Island. The scenes were collected on Dec. 24, 2016 and Jan. 31, 2017, identified here as Dec16 and Jan17. The sampled pixel and line spacing were 4.7 and 4.7 m for scene Dec16, and 4.7 and 5.1 m for scene Jan17, respectively. Fig. 2 depicts the Pauli RGB composites (red: $|HH-VV|$; green: $2|HV|$; blue $|HH+VV|$, where HH, HV, and VV are the QP intensity values) along with the ground truth maps of the scenes.

Over each scene, CIS experts assigned class labels to pixels via the MAGIC software [38]. Based on the sample pixels, each of the ground truth maps was generated from an oversegmentation that was manually labeled. The incidence angle varies between 31° and 34° for scene Dec16, and 38° and 41° for scene Jan17. The scenes have a large overlap; however, the ice types in the scenes vary from one scene to the other. While scene Dec16 consists of different ice types including new ice (NI), young ice (YI), first-year ice (FYI), and multiyear ice (MYI), due to the freeze-up process, scene Jan17 includes only FYI and MYI.

The full QP images were used to synthesize the MLC CP coherence matrix data via an RCM-data simulator [1]. The simulator uses elements of the full QP scattering matrix to construct the complex CP measurement vector, (1). The measurement vector was then used to generate the coherence matrix which was then resampled based on each beam mode of the RCM. Here, the CP coherence matrix data are in the medium resolution RCM mode with the pixel spacing of 50 m$\times$50 m (range$\times$ azimuth). A "box-car" averaging with window size of 9×9 is also applied on the data which is used as the input to the unsupervised segmentation algorithm. The region-based nature of CP-IRGS method makes it less sensitive to the speckle noise,

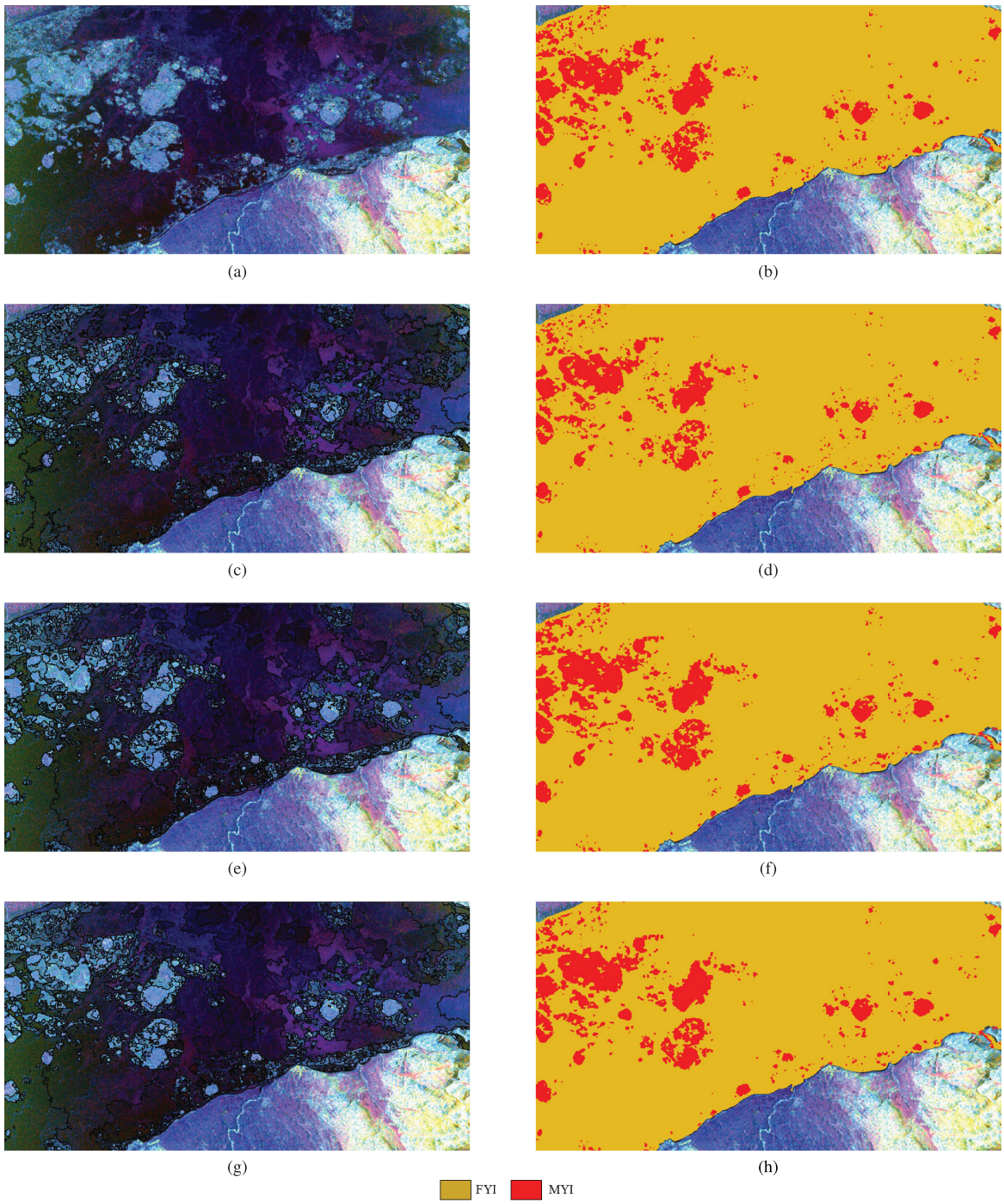

Fig. 5. Scene Jan17. (a) $M-\chi$ decomposition RGB composite; R $=\sqrt{(mS_0-S_3)/2}$; $G=\sqrt{S_0(1-m)}$; $B=\sqrt{(mS_0+S_3)/2}$, where S_0, S_1, S_2, S_3 are the Stokes parameters and $m=\sqrt{S_1^2+S_2^2+S_3^2}/S_0$ is the degree of polarization. (b) Ground truth, the unsupervised segmentation boundaries overlaid on top of $M-\chi$ RGB image, and the labeled images overlaid on top of land masks for the cases. (c) and (d) Unsupervised IRGS segmentation using RH and RV intensity images. (e) and (f) Unsupervised CP-IRGS segmentation using VFG method. (g) and (h) Unsupervised CP-IRGS segmentation using CR-based method.

and the value of L is set to one which means no multilooking is performed. In this manner, the image boundaries are more preserved in the segmentation results.

VII. Results and Analyses

The results of the unsupervised segmentation methods, the labeled images, and the quantitative assessments of the methods are provided in this section. First, using a simulated MLC CP image, and, second, using the two MLC CP images described in Section VI-B, we compare the three segmentation methods in terms of accuracy as well as the level of oversegmentation.

A. Results Using the Simulated MLC CP Data

Here, the results of the simulated MLC CP scene including the unsupervised segmentation images as well as their corresponding labeled images are provided. The $M-\chi$ decomposition

RGB composite [35] image of the scene is shown in Fig. 3(a). The results of the unsupervised segmentation methods in the three cases described in Section V overlaid on the RGB image as well as their corresponding labeled images are also presented in Fig. 3. All the three segmentation methods provided relatively accurate and identical results as shown in Fig. 3 and also supported by the quantitative results in Table II where accuracy in the three cases does not significantly vary from one method to the other.

According to the values OA, κ, and the total number regions, CP-IRGS provides more accurate results with less number of regions than the original IRGS segmentation using RH and RV intensities (Case 1). As delineated in ovals in Fig. 3(e)–(h), a fairly large number of FYI pixels in the middle of the scene are mislabeled as YI using original IRGS. This is also demonstrated in the relatively low accuracy of YI class for this case, 80.03%, as seen in Table II. The performance of CP-IRGS using VFG- and CR-based methods indicates no significant difference where the VFG method provides higher accuracy, however, larger number of regions than the CR-based approach as seen in Table II.

B. Results of the MLC CP Data

Since scene Dec16 consists of different ice types, this scene is more challenging than scene Jan17 for segmentation. As labeled in Fig. 2 and as shown in the ground truth image of scene Dec16 in Fig. 4(b), the areas covered by YI have totally different radar backscatter across the scene. Also, the ice types YI and FYI in the left part of the scene are very similar in backscatter. However, scene Jan17 only consists of FYI and MYI that seem to be much more distinguishable for the segmentation algorithm. In Fig. 4, the $M-\chi$ decomposition image of scene Dec16, the ground truth, and the unsupervised segmentation results, as well as the labeled images to the real ice types, are provided for the three different methods in Cases 1, 2, and 3 discussed in Section V.

As seen in the highlighted ovals in the labeled images in Fig. 4, the results of the CP-IRGS algorithm [Fig. 4(f) and (h)] provide better discrimination between YI and FYI classes all over the scene compared to the IRGS results using RH and RV intensities [Fig. 4 (d)]. However, there are some misclassified areas highlighted in the left part of the scene for the results of the CP-IRGS algorithm [Fig. 4 (f) and (h)]. Although the segmentation images by the IRGS algorithm using RH and RV intensities in Fig. 4(c) is much more oversegmented than the CP-IRGS segmentation images in Fig. 4(e) and (g), the CP-IRGS algorithm produces more accurate labeled images than the IRGS algorithm, as supported by the accuracy values in Table II. This demonstrates that the CP-IRGS algorithm produces segmentation classes that are more homogeneous than those in the segmentation by the original IRGS algorithm using RH and RV intensities.

In other words, some segmentation classes produced by the original IRGS algorithm using only RH and RV intensities include multiple ice types (are not purely from one ice type), and the majority voting process of labeling assigns only one ice type to all the regions in the segmentation class. However, the CP-IRGS algorithm produces more pure segmentation classes by leveraging the statistical characteristics of the MLC CP coherence data. Moreover, for scene Dec16, the CP-IRGS using CR produces slightly better labeling results than the CP-IRGS method using VFG (slightly higher OA and smaller number of regions using CR-based method than the VFG method).

The unsupervised segmentation and the labeled images for scene Jan17 are also shown in Fig. 5. All the three segmentation methods provide highly accurate discrimination between the two classes FYI and MYI in the scene. This is because this scene only consists of two ice types that are easily distinguishable by the segmentation algorithms due to the noticeable backscatter difference between classes. Thus, the phase information provided by the MLC CP data might be unnecessary particularly for this scene, and the original IRGS using only RH and RV intensities produces highly accurate results.

Table III also shows the segmentation performance using $M-\chi$ parameters in comparison with using CP intensities. Two of the three $M-\chi$ parameters that were more discriminative (the parameters G and B from $M-\chi$ RGB composite) were selected. These parameters were then used in Case 1 and Case 2 experiments. In particular, in Case 1, $M-\chi$ parameters G and B were used in the standard IRGS algorithm, and in Case 2, these parameters were used in the VFG method. According to Table III, the accuracy-based assessment of the comparison results demonstrated that $M-\chi$ parameters do not consistently provide better results than CP intensities. Investigation of using other CP-derived parameters in unsupervised segmentation remains as a line of future work.

VIII. Conclusion

A region-based unsupervised segmentation algorithm dedicated to the MLC CP coherence data is proposed in this article. The algorithm is structured based on a previous unsupervised algorithm called IRGS. First, the statistical properties of the MLC CP coherence data were described and was shown that, similar to the MLC QP covariance matrix data, the MLC CP coherence data follows a complex Wishart distribution. Second, the proposed CP-IRGS algorithm was formulated based on the MRF model, where both unary and pairwise potentials were modeled using MLC CP data. The CP-IRGS algorithm uses edge strength in the pairwise potential formulation for which a complex-ratio-based method has been proposed. In particular, the HLT statistic is used for calculating the edge strength in a bi-window configuration around each site on the image. Also, the algorithm involves a region-merging process which reduces the number of regions, and, in this manner, makes the optimization more efficient.

The experiments were conducted on a simulated CP scene generated based on the product model and a pair of RADARASAT-2 QP SLC images. Three different methods were tested: the IRGS method using RH and RV intensities, the CP-IRGS using VFG method, and the CP-IRGS using CR-based method. The results indicate that the CP-IRGS algorithm, which is particularly developed for the MLC CP coherence matrix data, performs the unsupervised segmentation in a more accurate manner than the original IRGS algorithm using RH and RV intensity images especially where the SAR scene consists

of multiple classes. Also, in general, the performance of the CP-IRGS algorithm using either VFG or CR-based methods were almost the same.

Future work involves developing a more sophisticated edge strength map calculation method that can leverage MLC CP coherence data. This can improve the performance unsupervised segmentation to a great extent. A reliable labeling process should be performed either after or during the unsupervised segmentation process. As future work, a supervised classification approach as labeling process can be either integrated into each iteration of the CP-IRGS algorithm or performed after the unsupervised segmentation. Different features may be used in the labeling process, including derived features using domain-specific knowledge such as intensity, texture, and shapes, and learned features using deep convolution neural networks (CNNs)-based methods. Designing CNNs-based semantic segmentation methods directly using complex values of MLC CP data can be another interesting future line of work.

REFERENCES

[1] F. Charbonneau *et al.*, "Compact polarimetry overview and applications assessment," *Can. J. Remote Sens.*, vol. 36, no. S2, pp. S 298--S315, 2010.

[2] F. J. Charbonneau *et al.*, "Meeting canadian user needs with the RADARSAT constellation mission's compact polarimetry mode: A summary assessment," Natural Resources Canada, *Ottawa. Geomatics Canada Open File*, no. 34, 2017.

[3] C. Lardeux *et al.*, "Classification of tropical vegetation using multifrequency partial SAR polarimetry," *IEEE Geosci. Remote Sens. Lett.*, vol. 8, no. 1, pp. 133–137, Jan. 2011.

[4] B. Zhang, X. Li, W. Perrie, and O. Garcia-Pineda, "Compact polarimetric synthetic aperture radar for marine oil platform and slick detection," *IEEE Trans. Geosci. Remote Sens.*, vol. 55, no. 3, pp. 1407–1423, Mar. 2017.

[5] R. Sabry and T. L. Ainsworth, "SAR compact polarimetry for change detection and characterization," *IEEE J. Sel. Topics Appl. Earth Observ. Remote Sens.*, vol. 12, no. 3, pp. 898–909, Mar. 2019.

[6] R. K. Raney, "Hybrid-polarity SAR architecture," *IEEE Trans. Geosci. Remote Sens.*, vol. 45, no. 11, pp. 3397–3404, Nov. 2007.

[7] J.-C. Souyris, P. Imbo, R. Fjortoft, S. Mingot, and J.-S. Lee, "Compact polarimetry based on symmetry properties of geophysical media: The $\frac{\pi}{4}$ mode," *IEEE Trans. Geosci. Remote Sens.*, vol. 43, no. 3, pp. 634–646, Mar. 2005.

[8] T. Ainsworth, J. Kelly, and J.-S. Lee, "Classification comparisons between dual-pol, compact polarimetric and quad-pol SAR imagery," *ISPRS J. Photogrammetry Remote Sens.*, vol. 64, no. 5, pp. 464–471, 2009.

[9] A. Buono, F. Nunziata, M. Migliaccio, and X. Li, "Polarimetric analysis of compact-polarimetry SAR architectures for sea oil slick observation," *IEEE Trans. Geosci. Remote Sens.*, vol. 54, no. 10, pp. 5862–5874, Oct. 2016.

[10] R. K. Raney, "Synthetic aperture radar hybrid-polarity method and architecture for obtaining the Stokes parameters of a backscattered field," Jun. 29 2010, US Patent 7746267.

[11] J.-C. Souyris and S. Mingot, "Polarimetry based on one transmitting and two receiving polarizations: The $\frac{\pi}{4}$ mode," in *Proc. IEEE Int. Geosci. Remote Sens. Symp.*, 2002, pp. 629–631.

[12] R. Raney, "Comparing compact and quadrature polarimetric SAR performance," *IEEE Geosci. Remote Sens. Lett.*, vol. 13, no. 6, pp. 861–864, Jun. 2016.

[13] Q. Yu and D. A. Clausi, "IRGS: Image segmentation using edge penalties and region growing," *IEEE Trans. Pattern Anal. Mach. Intell.*, vol. 30, no. 12, pp. 2126–2139, Dec. 2008.

[14] Q. Yu and D. Clausi, "SAR sea-ice image analysis based on iterative region growing using semantics," *IEEE Trans. Geosci. Remote Sens.*, vol. 45, no. 12, pp. 3919–3931, Dec. 2007.

[15] F. Li, D. A. Clausi, L. Xu, and A. Wong, "ST-IRGS: A region-based self-training algorithm applied to hyperspectral image classification and segmentation," *IEEE Trans. Geosci. Remote Sens.*, vol. 56, no. 1, pp. 3–16, Jan. 2018.

[16] A. Qin and D. A. Clausi, "Multivariate image segmentation using semantic region growing with adaptive edge penalty," *IEEE Trans. Image Process.*, vol. 19, no. 8, pp. 2157–2170, Aug. 2010.

[17] P. Yu, A. Qin, and D. A. Clausi, "Unsupervised polarimetric SAR image segmentation and classification using region growing with edge penalty," *IEEE Trans. Geosci. Remote Sens.*, vol. 50, no. 4, pp. 1302–1317, Apr. 2012.

[18] G. A. Seber, *Multivariate Observations*. Hoboken, NJ, USA: John Wiley and Sons, 2009, vol. 252.

[19] C. Oliver and S. Quegan, *Understanding Synthetic Aperture Radar Images*. Rijeka, Croatia: SciTech Publishing, 2004.

[20] J.-S. Lee and E. Pottier, *Polarimetric Radar Imaging: From Basics to Applications*. Boca Raton, FL, USA: CRC press, 2009.

[21] S. Cloude, *Polarisation: Applications in Remote Sensing*. London, U.K.: Oxford University Press, 2010.

[22] N. R. Goodman, "Statistical analysis based on a certain multivariate complex gaussian distribution (an introduction)," *Ann. Math. Statist.*, vol. 34, no. 1, pp. 152–177, 1963.

[23] A. C. Frery *et al.*, "Models for synthetic aperture radar image analysis," *Resenhas Instituto Matemática Estatística Universidade São Paulo*, vol. 4, no. 1, pp. 45–77, 1999.

[24] A. P. Doulgeris, S. N. Anfinsen, and T. Eltoft, "Classification with a non-gaussian model for PolSAR data," *IEEE Trans. Geosci. Remote Sens.*, vol. 46, no. 10, pp. 2999–3009, Oct. 2008.

[25] A. C. Frery, A. H. Correia, and C. d. C. Freitas, "Classifying multifrequency fully polarimetric imagery with multiple sources of statistical evidence and contextual information," *IEEE Trans. Geosci. Remote Sens.*, vol. 45, no. 10, pp. 3098–3109, Oct. 2007.

[26] S. Z. Li, *Markov Random Field Modeling in Image Analysis*. Berlin, Germany: Springer Science and Business Media, 2009.

[27] L. Vincent and P. Soille, "Watersheds in digital spaces: An efficient algorithm based on immersion simulations," *IEEE Trans. Pattern Anal. Mach. Intell.*, no. 6, pp. 583–598, Jun. 1991.

[28] H.-C. Lee and D. R. Cok, "Detecting boundaries in a vector field," *IEEE Trans. Signal Process.*, vol. 39, no. 5, pp. 1181–1194, May 1991.

[29] R. Touzi, A. Lopes, and P. Bousquet, "A statistical and geometrical edge detector for SAR images," *IEEE Trans. Geosci. remote Sens.*, vol. 26, no. 6, pp. 764–773, Nov. 1988.

[30] C. Oliver, D. Blacknell, and R. White, "Optimum edge detection in SAR," *IEE Proc. Radar Sonar Navigation*, vol. 143, no. 1, pp. 31–40, 1996.

[31] J. Schou, H. Skriver, A. A. Nielsen, and K. Conradsen, "CFAR edge detector for polarimetric SAR images," *IEEE Trans. Geosci. Remote Sens.*, vol. 41, no. 1, pp. 20–32, Jan. 2003.

[32] V. Akbari, S. N. Anfinsen, A. P. Doulgeris, T. Eltoft, G. Moser, and S. B. Serpico, "Polarimetric SAR change detection with the complex Hotelling–Lawley trace statistic," *IEEE Trans. Geosci. Remote Sens.*, vol. 54, no. 7, pp. 3953–3966, Jul. 2016.

[33] M. Ghanbari and V. Akbari, "Unsupervised change detection in polarimetric SAR data with the hotelling-lawley trace statistic and minimum-error thresholding," *IEEE J. Sel. Topics Appl. Earth Observ. Remote Sens.*, vol. 11, no. 12, pp. 4551–4562, Dec. 2018.

[34] X. Descombes, R. D. Morris, J. Zerubia, and M. Berthod, "Estimation of Markov random field prior parameters using Markov chain Monte–Carlo maximum likelihood," *IEEE Trans. Image Process.*, vol. 8, no. 7, pp. 954–963, Jul. 1999.

[35] R. K. Raney, J. T. Cahill, G. Patterson, and D. B. J. Bussey, "The m-chi decomposition of hybrid dual-polarimetric radar data with application to lunar craters," *J. Geophysical Research: Planets*, vol. 117, no. E12, 2012.

[36] S. Leigh, Z. Wang, and D. A. Clausi, "Automated ice-water classification using dual polarization SAR satellite imagery," *IEEE Trans. Geosci. Remote Sens.*, vol. 52, no. 9, pp. 5529–5539, Sep. 2014.

[37] M. Ghanbari, D. A. Clausi, L. Xu, and M. Jiang, "Contextual classification of sea-ice types using compact polarimetric SAR data," *IEEE Trans. Geosci. Remote Sens.*, vol. 57, no. 10, pp. 7476–7491, Oct. 2019.

[38] D. A. Clausi, A. Qin, M. Chowdhury, P. Yu, and P. Maillard, "MAGIC: MAp-guided ice classification system," *Can. J. Remote Sens.*, vol. 36, no. S1, pp. S 13–S25, 2010.

Mohsen Ghanbari (Student Member, IEEEE) received the B.Sc. degree in geomatics engineering from the University of Tehran, Tehran, Iran, in 2012, and the M.Sc. degree in remote sensing from the Khajeh Nasir Toosi University of Technology, Tehran, Iran, in 2015. He is currently working toward the Ph.D. degree in systems design engineering with the University of Waterloo, Waterloo, ON, Canada.

His research interests include computer vision and machine learning, with main focus on synthetic aperture radar image processing.

David A. Clausi received the Ph.D. degree in systems design engineering from the University of Waterloo, Waterloo, ON, Canada, in 1996.

Afterward, he worked in medical imaging at Mitra Imaging, Waterloo, ON, Canada. He started his academic career in 1997 as an Assistant Professor in Geomatics Engineering with the University of Calgary, Canada. In 1999, he joined the University of Waterloo, where he is currently a Professor who specializes in the field of intelligent systems and is also the Associate Dean Research & External Partnerships with the Faculty of Engineering. He has numerous contributions, and has authored or coauthored published in refereed journal and conference papers primarily in remote sensing, computer vision, image processing, and algorithm design.

Dr. Clausi was the Co-Chair of IAPR Technical Committee 7 - Remote Sensing during 2004–2006. He was the recipient of many scholarships, paper awards, research awards, teaching excellence awards, and his efforts have led to successful commercial implementations, culminating in the creation and sale of a high-tech company.

Linlin Xu (Member, IEEE) received the B.Eng. and M.Sc. degrees in geomatics engineering from the China University of Geosciences, Beijing, China, in 2007 and 2010, respectively, and the Ph.D. degree in geography from the Department of Geography and Environmental Management, University of Waterloo, Waterloo, ON, Canada, in 2014.

He was an Associate Professor with the China University of Geosciences for two years. He is currently a Research Assistant Professor with the Department of Systems Design Engineering, University of Waterloo. He has authored or coauthored various papers published in high-impact remote sensing journals and conferences. His research interests include hyperspectral and synthetic aperture radar data processing, and their applications in various environmental applications.